

Reflection waveforms occurring in bistatic radar testing of columns and tree trunks



Jana Ježová*, Julie Harou, Sébastien Lambot

Université catholique de Louvain, Louvain-la-Neuve, Belgium

HIGHLIGHTS

- Bistatic radar system analysis.
- Analysis of radar wave propagation in cylinders.
- Numerical, laboratory and real radar data.
- Tree trunk and concrete column analysis.

ARTICLE INFO

Article history:

Received 22 December 2017

Received in revised form 5 April 2018

Accepted 13 April 2018

Keywords:

Ground-penetrating radar

Non-destructive testing

gprMax2D

Trees

Columns

ABSTRACT

Ground-penetrating radar is a non-destructive inspection device which is not often applied to cylindrical media. In this paper, we extend our previous analyses of monostatic GPR waveforms to two bistatic radar configurations for cylindrical objects: 1) Single-offset radar system, where two antennas are simultaneously rotating around the cylinder, 2) multi-offset radar system, where only a receiving antenna is rotating around it. Analyses were performed through numerical experiments with gprMax2D, straight-ray analytical solutions, laboratory and real case studies. The complex real case studies highlighted the benefit of combining bistatic and monostatic radar data acquisitions to better resolve unknown internal structures.

© 2018 Elsevier Ltd. All rights reserved.

1. Introduction

Ground-penetrating radar (GPR) is a powerful non-invasive tool for under-surface structures detection. Its functioning is based on scattering of electromagnetic waves that are emitted from a transmitting antenna and collected by a receiving antenna [1–3]. GPR has been used in many fields, such as civil and transport engineering [4–6], environmental applications [7–10], archaeology [11–13], and geophysics [14–16]. Most of these applications involve planar model configurations. For those cases, the interpretation of GPR images is well described and relatively intuitive. Nevertheless, data collection for other shapes, such as cylinders (columns, tree trunks, etc.), is more complex to interpret [17]. The context of our research is related to tree trunk inspection with GPR in order to predict tree trunk collapses caused by voided wood. For this application, a circumferential data acquisition is needed. Therefore, this paper is

dedicated to the analysis of electromagnetic wave propagations in cylinders and resulting GPR images.

In a planar GPR image, one can observe hyperbolic reflection curves originating from buried objects (rebars, pipes, landmines, etc.) [18–21] or continuous reflection curves indicating different layers (road layers, groundwater table, etc.) [22–24]. However, in cylinders the electromagnetic waves propagate differently due to their curvature and, therefore, many cases of multiple reflections from the cylinder-air interface occur. In our previous research [25], we described reflection curves occurring in cylinders using a monostatic radar system (a single antenna for transmitting and receiving). Yet, in a bistatic radar system (one transmitting and one receiving antenna), it is possible to observe a series of interesting wave propagation paths. A bistatic acquisition also provides additional information about the inspected medium thanks to a different accessibility of the antennas to the medium. The reflection curves do highlight not only the position of an under-surface object, they can also be used to determine the electromagnetic properties of the medium. Therefore, it is worth to recognize as many reflection curves as possible in order to collect more

* Corresponding author.

E-mail address: jana.jezova@uclouvain.be (J. Ježová).

information about the investigated medium. Reflection curves occurring in cylindrical structures were observed by Nuzzo and Quarta [26] and Bonomo et al. [27] who studied protection of cultural heritage. Persico and Soldovieri [28] and Leucci et al. [29,30] studied the influence of the use of the monostatic and multistatic configurations on column reconstruction tomography. GPR inspection of tree trunks was performed by, e.g., Nicolotti et al. [31], Lorenzo et al. [32] and al Hagrey [33].

The objective of this paper is to analyse reflection curves appearing in radar images of cylindrical structures obtained with the use of the GPR in bistatic mode (transmission). To make the link with our previous research, we compare our new results with the data collected with the use of a monostatic radar system. Specifically, both single-offset mode, where the antennas are opposite to each other and rotate around the object with fixed spacing, and multi-offset mode, where the transmitter stays at one position and the receiver rotates around the object, were considered. Firstly, we performed numerical simulations using the gprMax2D software [34,35], which solves the two-dimensional Maxwell equations using the Finite-Difference Time-Domain (FDTD) method [36] and which is specifically dedicated to GPR applications. Then, several possible propagation paths were observed and analysed with the help of snapshots of the electromagnetic field propagation made with gprMax2D. Using the straight-ray approximation, we analytically derived the shapes of the reflection curves of a circular inhomogeneity in the cylinder for easier determination of its position, shape and size, and we compared them with the reflections occurring in the numerical simulations and real radar images. We also performed laboratory measurements of a tree trunk model in the lab. Finally, we performed radar measurements for two real case studies to compare the real data with the simulated ones and those obtained in the laboratory. Specifically, we inspected a reinforced concrete column and a tree trunk with a cavity. For these measurements, we used a frequency-domain monostatic radar system and both bistatic radar configurations described above.

2. Numerical simulations

To better understand data obtained by a circumferential data acquisition scheme, we performed numerical simulations of radar measurements around a simple cylindrical model. Fig. 1 shows the two considered radar configurations: (a) with the transmitter and the receiver opposite to each other and rotating around the medium, (b) with the transmitter at a fixed position and the receiver rotating around the medium. Similarly to our previous research [25], our model was composed of two cylinders filled with sand and air, respectively.

To examine possible GPR images for this radar configuration, we used the gprMax2D (open source) software [34,35] which simu-

lates propagation of electromagnetic waves and is specially dedicated to GPR applications. For the simulations, the relative permittivity of the sand was set to $\epsilon_r = 3$ and electric conductivity was set to $\sigma = 0\text{S/m}$. The operating source was a Ricker wavelet with a centre frequency $f_c = 900\text{ MHz}$. The spatial resolution of the numerical model geometry in the x and y directions was set to 2,5 mm. For all our GPR images, we applied an exponential gain function.

In order to understand the simulated GPR images, the propagation paths were analysed and possible reflection waveforms were derived. To inspect possible propagation paths in the cylinder, we observed the time-lapse electromagnetic field distribution simulated by gprMax2D.

In our previous research, we observed two major ways of propagation as displayed in Fig. 2: 1) straight-ray, and 2) total internal reflection (TIR). The straight-ray approximation is a one-dimensional propagation of the signal which is a relatively good approximation for not very complex media. We used this term also for the direct multiple reflections and composed linear reflections described below. The TIR is a phenomenon occurring when a wave is scattered from electromagnetically denser medium to a less dense medium with an angle of incidence larger than the so-called critical angle. When these two conditions are fulfilled, the wave is fully reflected back to the medium with an angle which is identical in the opposite direction to the angle of incidence. In this case, the signal is reflected along the inner edge of the medium and its path has the shape of a regular polygon (from a pentagon up to a circle). In this paper, we represent the TIR as a circle or a part of a circle to show the path more easily in our images. Nevertheless, in the calculations, it was represented as a 5-sided regular polygon. This path was the most relevant for our setup as it was the shortest path avoiding internal voids. To express the reflection curves in the radargrams, simplified formulas in Eqs. (1) and (2) were used to obtain the propagation time of the signal:

$$v = \frac{c}{\sqrt{\epsilon_r}} \tag{1}$$

where v is the wave propagation velocity [m/s], c is the speed of light in vacuum [m/s], and ϵ_r is the relative permittivity of the medium [dimensionless].

$$t = \frac{d}{v} \Rightarrow t = \frac{\sqrt{\epsilon_r} \cdot d}{c} \tag{2}$$

where t is the propagation time [s] and d is the length of the propagation path [m].

Fig. 3 shows reflection curves simulated for a monostatic radar system, where interfaces 1 and 2 are the closest and the furthest points on the void edge, respectively, interface 3 is the opposite side of the medium, and TIR is the total internal reflection in the model (see Fig. 2a). The TIR continues its propagation along the internal edge of the medium and if the inner edge acted as a perfect

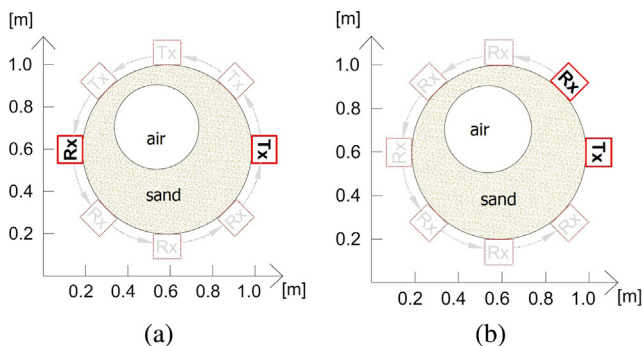


Fig. 1. Model geometry used for the numerical experiments with the single-offset (a) and multi-offset (b) radar antenna configurations.

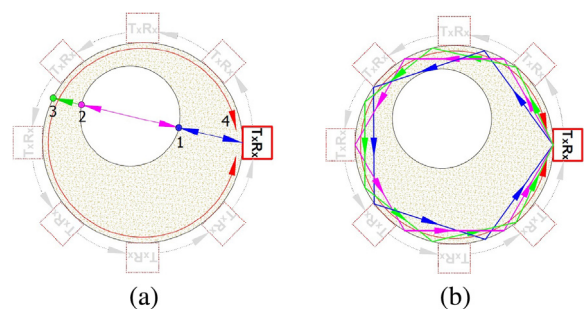


Fig. 2. Main wave propagation paths obtained by monostatic GPR: (a) 4 paths of straight-ray propagation, (b) detailed total internal reflection (TIR).

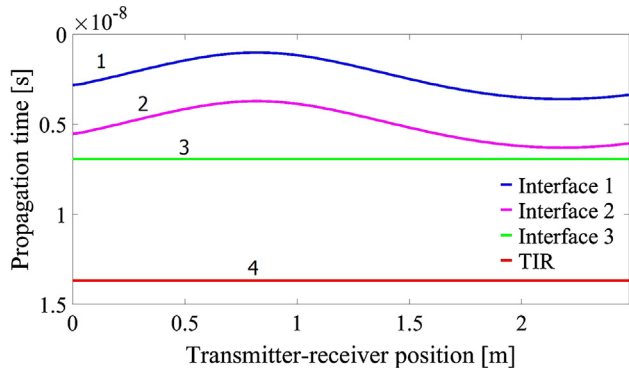


Fig. 3. Reflection curves obtained by a monostatic GPR system for the cylindrical configuration shown in Fig. 2.

mirror, in a lossless medium it would never stop. In that respect, the TIR would be visible as a multiple reflection if we displayed larger propagation times. In this paper, only the first reflection originating from the TIR is presented.

Due to the intricacy of the GPR images obtained with two antennas in the transmission mode, it is very helpful to closely observe the propagation of the electromagnetic field in our model. Knowing the properties and behaviour of the electromagnetic field, we can describe and analytically express relatively precisely every reflection curve which should theoretically appear in a GPR image. The analytical curves were shifted by ≈ 1 ns compared with the curves in the numerical simulations due to the shifted time zero in gprMax2D.

2.1. Single-offset mode

Fig. 4 shows the radar image obtained for the first scenario, namely, with the transmitting and receiving antennas opposite to each other and simultaneously turning around the cylinder. One can observe two strong reflection curves: 1) a relatively constant reflection highlighted by the green arrow t_1 (≈ 5 ns), and 2) a strong constant reflection highlighted by the magenta arrow t_4 (≈ 8 ns). In the radargram, another two relatively weak reflections are visible. They are pointed out by the red and the blue arrows (t_2 and t_3).

Fig. 5 shows the distribution of the electromagnetic field in our cylindrical model. The values of the electric field strength in [V/m] were normalized following Eq. (3) in order to express the values in interval $[-1, 1]$.

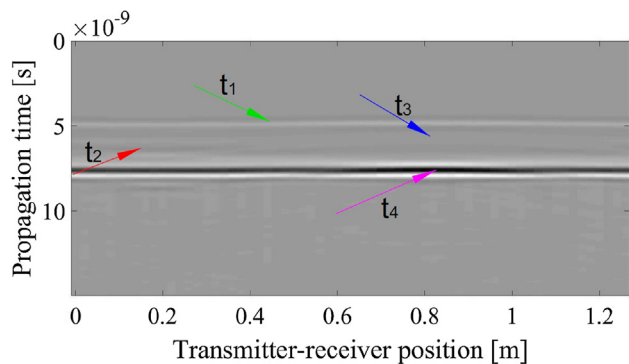


Fig. 4. Numerical simulation using gprMax2D for the first bistatic radar configuration, where both antennas are rotating around the medium (see Fig. 1a).

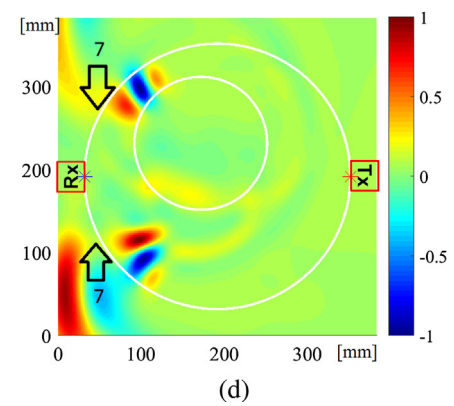
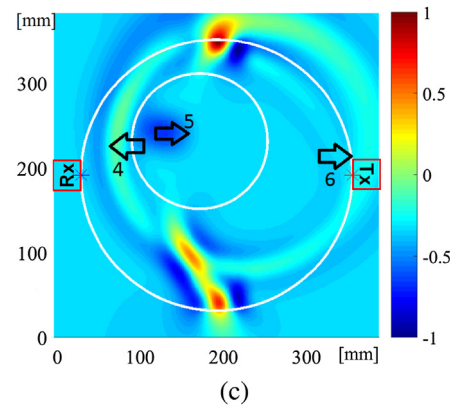
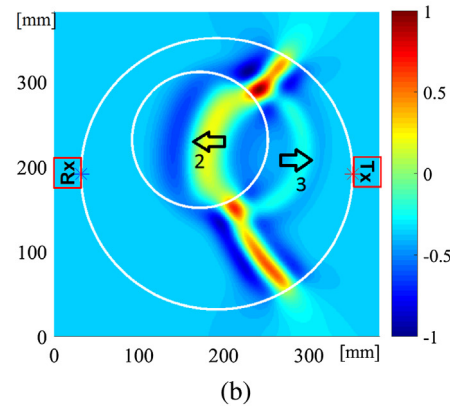
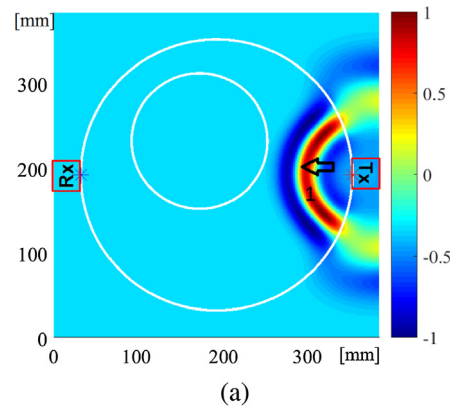


Fig. 5. Normalized distribution of the electric field simulated using gprMax2D at four different propagation times, namely, (a) 2.0 ns, (b) 3.3 ns, (c) 4.3 ns and (d) 6.0 ns.

$$E_{z,norm}(x,y) = \frac{2 \cdot E_z(x,y) - 2 \cdot E_{z,min}}{E_{z,max} - E_{z,min}} - 1 \quad (3)$$

where $E_{z,norm}(x,y)$ is the normalized value of the electric field strength [dimensionless] in the z direction at a position $[x,y]$, $E_z(x,y)$ is the electric field strength [V/m] in the z direction at a position $[x,y]$, $E_{z,min}$ and $E_{z,max}$ are the minimum and maximum values of the electric field strength [V/m], respectively.

In Fig. 5a corresponding to a propagation time of 2 ns, the signal 1 is transmitted from the transmitter and mainly continues straightly through the medium. In Fig. 5b corresponding to 3.3 ns, wave 2 hits the border of the void and propagates through it towards its centre, whilst the reflected part 3 propagates back towards the transmitter. In Fig. 5c corresponding to 4.3 ns, wave 2 hits the void border and one part of it (4) continues towards the receiver, whilst the other part of the signal (5) is reflected backwards. At the same time, wave 6 hits the edge of the medium and a part of it is reflected back to the medium and a part of it is refracted. In Fig. 5d corresponding to 6 ns, the TIR (7) propagates along the edge of the model and continues towards the receiver. Fig. 6 shows 4 major simplified propagation paths in our model which were observed in the electromagnetic field snapshots shown in Fig. 5.

We derived analytical equations for each propagation path. Fig. 7 shows the geometry of the configuration for deriving the lengths of the propagation paths. Eq. (4) describes the coordinates $p_x(\theta)$ and $p_y(\theta)$ on the edge of the model with x_1 and y_1 defining the centre of the model [m] and R_1 being the radius of the model [m]. Eq. (5) describes the distance d depending on angle θ (in Fig. 7 it is represented for θ equal to 0 and π), where x_2 and y_2 are the coordinates of the void [m] and R_2 is the radius of the void [m].

$$p_x(\theta) = x_1 + R_1 \cos \theta, \quad p_y(\theta) = y_1 + R_1 \sin \theta \quad (4)$$

$$d(\theta) = \sqrt{(p_x(\theta) - x_2)^2 + (p_y(\theta) - y_2)^2} - R_2 \quad (5)$$

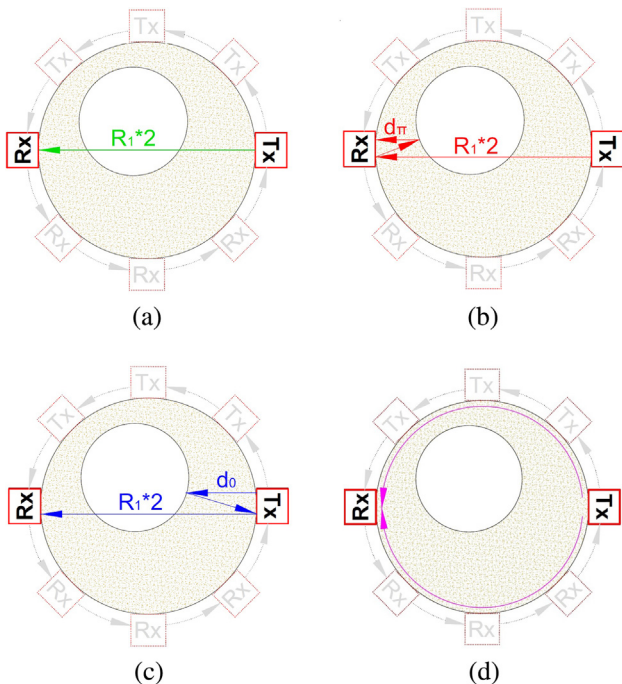


Fig. 6. Simplified straight-ray paths for the opposite transmission antenna configuration (first case of the bistatic radar system).

Fig. 8 shows 4 main reflection curves derived according to the propagation paths displayed in Fig. 6. Eqs. 6,7 below describe the propagation time t [s] with the relative permittivity of the medium ϵ_r [dimensionless], and the speed of light c [m/s].

Fig. 6a shows a straight-ray propagation going directly from the transmitter Tx to the receiver Rx. This arrival time t_1 is displayed in green colour as a constant reflection curve in Fig. 8. The constant shape is caused by neglecting the refraction of the wave. This reflection curve is described by Eq. (6):

$$t_1 = \frac{\sqrt{\epsilon_r} \cdot R_1 \cdot 2}{c} \quad (6)$$

In Fig. 6b, the first multiple reflection between the cylinder edge and inner heterogeneity is shown. This reflection time t_2 is displayed in red colour in Fig. 8. Eq. (7) describes propagation time t_2 of this reflection [s] with d_π being the distance between the receiver and the void [m] for $\theta = \pi$.

$$t_2 = \frac{\sqrt{\epsilon_r} \cdot (R_1 \cdot 2 + d_\pi \cdot 2)}{c} \quad (7)$$

The path presented in Fig. 6c, which is expressed as the blue curve t_3 in Fig. 8, has similar character as the previous reflection. A multiple reflection occurs between the transmitter and the inner cavity. This reflection is nearly identical to the previous one but it is shifted by 180° . Therefore, the maximum of t_3 is reached at the same posi-

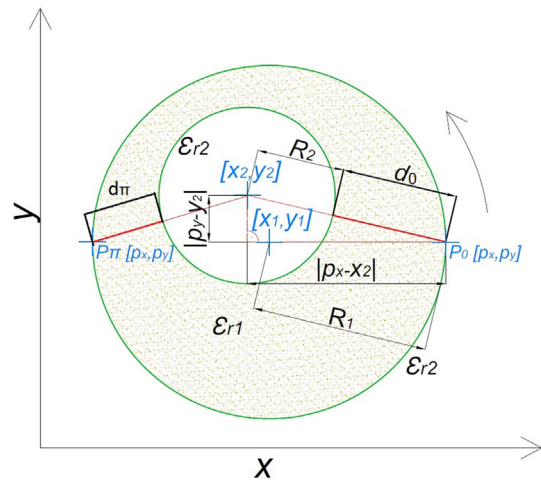


Fig. 7. Medium configuration with distance d of the void from the antenna (P_0, P_π) . ϵ_1 and ϵ_2 are the dielectric constants of sand and air, respectively. R_1 and R_2 are the radii of the medium and the void, respectively.

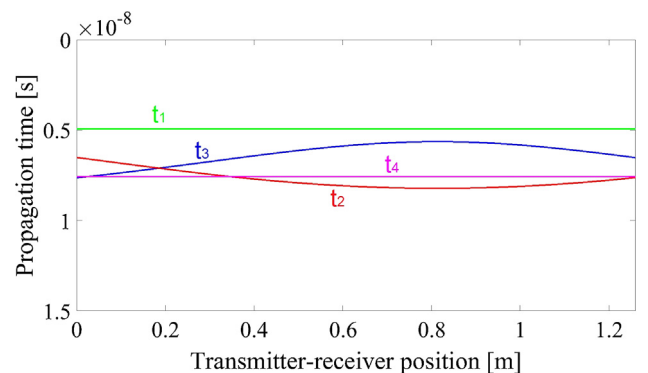


Fig. 8. Analytic reflection curves for the single-offset mode, where both antennas are rotating around the medium (see Fig. 1a).

tion as the minimum of t_2 and vice versa. Eq. (8) describes the propagation time t_3 of this reflection [s] with d_0 being the distance [m] for $\theta=0$.

$$t_3 = \frac{\sqrt{\epsilon_r} \cdot (R_1 \cdot 2 + d_0 \cdot 2)}{c} \tag{8}$$

The last propagation path shown in Fig. 6d is the TIR which is reflected from the edge back to the medium and continues in both directions along its boundary to the opposite side of the medium. In that position, both waves interfere and are recorded by the receiving antenna. In Fig. 8 it is represented by the magenta line t_4 which is constant because the propagation path is identical for all positions along the medium boundary. The shortest propagation path has a shape of a regular 5-sided polygon. Its perimeter p is described by Eq. (9), where n is the number of the polygon vertices (in our case 5). The reflection time t_4 is described by Eq. (10), where p is the distance of the path expressed as a half of the perimeter of a regular polygon:

$$p = 2 \cdot n \cdot R_1 \sin(\pi/n) \tag{9}$$

$$t_4 = \frac{\sqrt{\epsilon_r} \cdot p}{c \cdot 2} \tag{10}$$

Fig. 9 shows the simulated GPR image together with the derived reflection curves. In spite of neglecting refraction of the signal t_1 , the derived curve fits very well to the GPR image in terms of position and shape. The complexity of the medium and the difference of the permittivities is not large enough to strongly influence the direction of the propagation. Thus, the reflection time is constant. In the simulated GPR image, the TIR is the strongest reflection due to the full internal reflections in synthetic conditions. Its intensity overshadows the reflection curves caused by the internal inhomogeneity, namely, corresponding to t_2 and t_3 .

2.2. Multi-offset mode

The second radar configuration we analysed consisted of a transmission setup with the transmitting antenna at a fixed position and the receiving antenna rotating around the medium. Fig. 10 shows the simulation of the second configuration. The strongest reflection in the radargram is the cross-shaped reflection pointed out by the red and orange arrows (t_8 and t_9), respectively. Then, we can see a very clear sinusoidal reflection curve marked by the blue arrow t_5 (around 4–5 ns). Another visible reflection in the simulated image is the one pointed out by the cyan arrow t_6 (around 5–7 ns). It is mainly visible in the ranges 0–0.8 m and 1.6–2.5 m. The green arrow t_{10} points at the reflection appearing

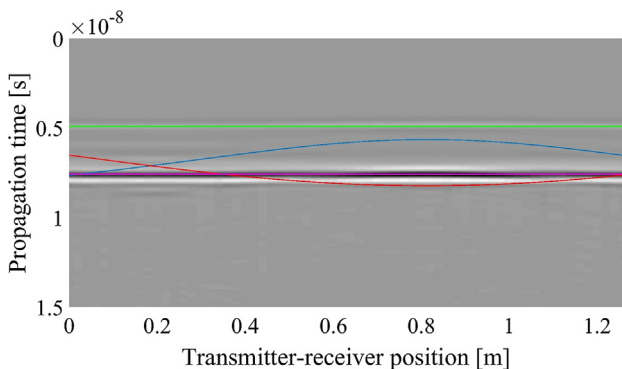


Fig. 9. Numerical simulation of the single-offset bistatic radar measurement (both antennas are rotating around the medium as in Fig. 1a) with the derived curves.

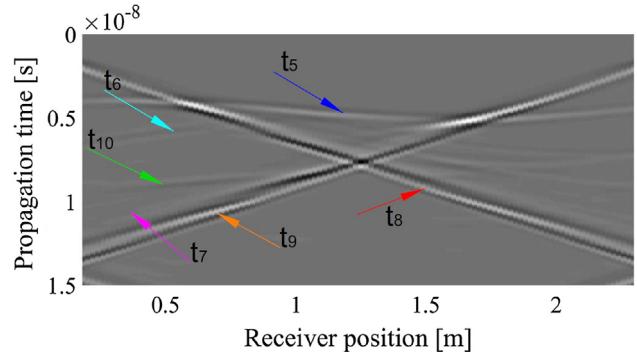


Fig. 10. Numerical simulation of the multi-offset bistatic radar measurement with the transmitter at a fixed position and the receiver rotating around the medium (see Fig. 1b).

from 8 to 9 ns. Finally, the cross shape reflection is influenced by a very weak reflection pointed out by the magenta arrow t_7 .

This radar setup is complicated by the varying angle of the direct path with respect to the medium geometry. In that case, refraction cannot be neglected anymore. For this setup the final GPR image is very complex and then, it was necessary to choose the main propagation paths very carefully. Fig. 11 shows 5 paths

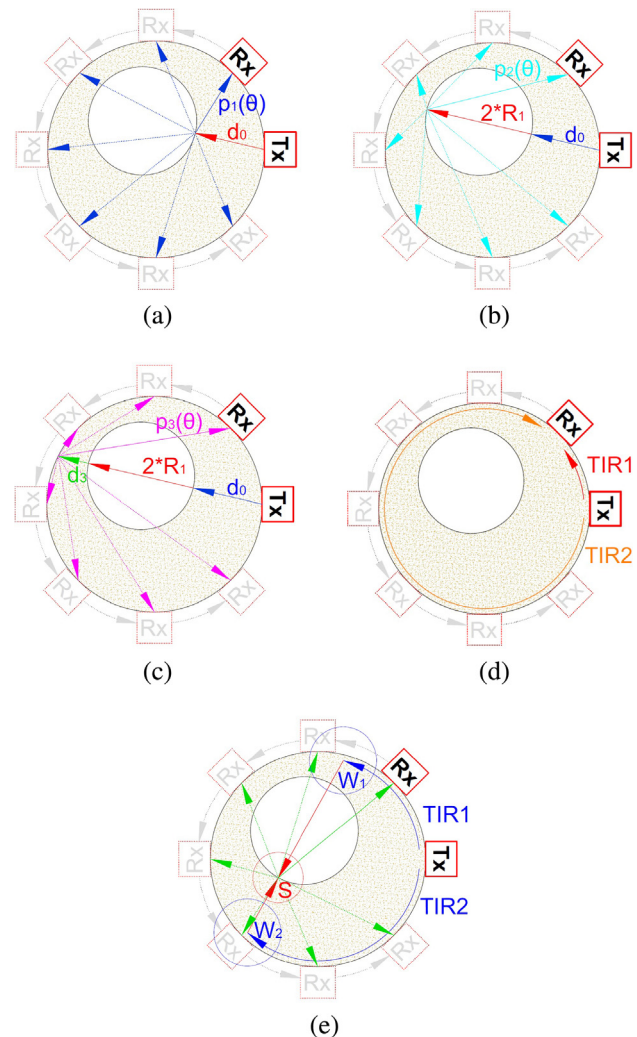


Fig. 11. Direct propagation paths for the second scenario, where the transmitter is fixed at one position and the receiver is rotating around the medium (see Fig. 1b).

of propagation in the multi-offset mode of the bistatic radar system according to the distribution of the electromagnetic field shown in Fig. 5. For each significant propagation path, an approximate equation was derived. All undescribed distances ($d_3, p_1(\theta), p_2(\theta), p_3(\theta)$) were derived using the Pythagorean theorem as well as $d(\theta)$ in Eq. (5). The resulting reflection curves are shown in Fig. 12.

Fig. 11a displays the direct propagation path corresponding to the blue reflection curve t_5 in Fig. 12. The distance d_0 between the void and the transmitting antenna is constant. At this point, the signal is partly reflected and partly refracted into the void from where it continues with its propagation through the air and then again through the sand. This reflection is described by Eq. (11), where p_1 is the distance [m] between the void and the receiver. When deriving the analytical expression of the curve, it was not straightforward to decide at which positions the receiver recorded a wave propagated through one or two media, thus, the transition between them shows two discontinuities. In Fig. 12 the refracted part (propagating through 2 media) of the signal (position 0.5–1.9 m) is indicated by dashed lines.

$$t_5 = \frac{\sqrt{\epsilon_r} \cdot (d_0 + p_1(\theta))}{c} \tag{11}$$

Another major propagation path we identified is shown in Fig. 11b. The origin of that path is the reflection at the second encountered void interface. From this point, the signal is again partly reflected and partly refracted. In Fig. 12, the reflection t_6 originating from this propagation path is highlighted by the cyan colour. The reflected part (0.8–1.6 m) is bounded by dashed lines. We expressed this reflection by Eq. (12), where $p_2(\theta)$ is the distance between the receiver and the opposite side of the void [m]:

$$t_6 = \frac{\sqrt{\epsilon_r} \cdot (d_0 + 2 \cdot R_2 + p_2(\theta))}{c} \tag{12}$$

Fig. 11c presents the next step of the wave propagation from Fig. 11b. The wave propagates through the medium with the void until it hits the opposite side of the medium. At that place, a part of the wave is scattered to the receiver. The reflection t_7 curve corresponding to this path is displayed in Fig. 12 as a magenta curve. It is described by Eq. (13), where d_3 is the distance between the void and the medium edges and $p_3(\theta)$ is the distance between the receiver and the other side of the medium:

$$t_7 = \frac{\sqrt{\epsilon_r} \cdot (d_0 + 2 \cdot R_2 + d_3 + p_3(\theta))}{c} \tag{13}$$

The next propagation path is the already mentioned TIR outlined in Fig. 11d. The reflection curves shown in Fig. 12 by red and orange lines appear as diagonal lines crossing each other due

to the change of the receiver position (angle θ). The reflections are linear because the TIR does not encounter any changes in the medium properties along the edge. The shortest propagation path has the shape of a regular 5-sided polygon. The reflections t_{8-9} are described by Eq. (14), where $p(\theta)$ is the distance of the path expressed as a part of the perimeter p of the regular polygon described in Eq. (9) according to the change of the angle θ :

$$t_{8-9} = \frac{\sqrt{\epsilon_r} \cdot (p(\theta))}{c} \tag{14}$$

The last presented propagation path of the signal is shown in Fig. 11e and it is illustrated by the green curve t_{10} in Fig. 12. Such a propagation path is not obvious. In order to find an explanation for the reflection curve visible in the simulation results, the spatial distribution of the electromagnetic field was studied in detail. It turned out that the origin of the reflection curve is the wave interaction in the area S in Fig. 11e. The propagation starts with the classical TIR going along the inner border of the medium. When it is at the level of the interface with the void in the upper section, a part of the signal is transmitted through the void. The same phenomenon occurs for the lower section of the model (see red arrows). The two signals interfere the void and the signal is scattered towards the receiver as a straight-ray propagation. To find the propagation path that would lead to such an interaction, a numerical scan through the parameter space was performed. The resulting equation of the propagation path has the same form as the basic Eq. (2) but it depends also on the position of points W1 and W2 in Fig. 11e. Their distance from the transmitter is 0.52 m ($\theta = 75^\circ$) for W1 and 0.9 m ($\theta = 230^\circ$) for W2. The approximate positions were determined by testing 62 randomly selected values from the intervals $\theta = 60 - 90^\circ$ and $\theta = 210 - 240^\circ$. The values were selected in such a way that they were separated by 1° so that the whole interval was covered by this survey.

Fig. 13 shows the simulated GPR image overlapped with the curves derived in this section. The blue curve t_5 , the cyan curve t_6 and the green curve t_{10} display a discontinuity for the position highlighted by dashed lines that corresponds to the transition between the sand and the air. The instantaneous change of values of the function at the border between the two regions is a trivial consequence of the choice of the analytical representation of a signal path. In our approximation, we assume that the propagations in the 2 regions are independent of each other and thus, at the region border the function abruptly changes as the relative permittivity changes, while the rest of the function remains identical. Nevertheless, even if there is some difference between simulation and our analytical representation of the reflection curve in the area around the air/sand border, the analytical curve agrees quite well with the

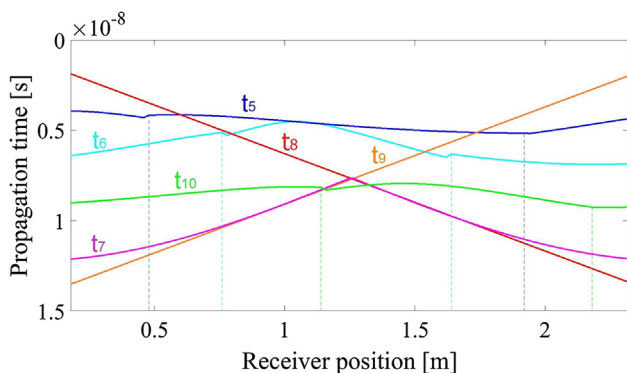


Fig. 12. Analytical reflection curves for the multi-offset mode with the transmitter at a fixed position and the receiver rotating around the medium (see Fig. 1b).

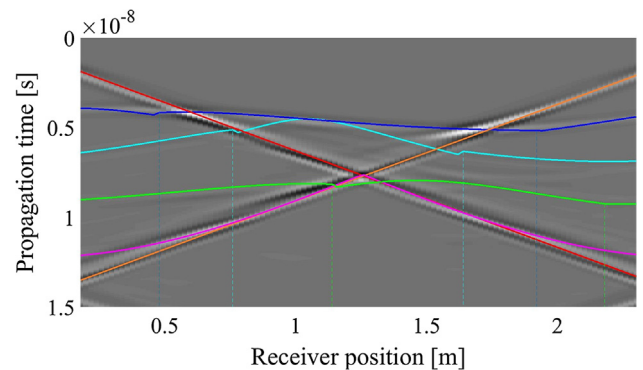


Fig. 13. Numerical simulation of the second bistatic radar measurement (with the transmitter at a fixed position and the receiver rotating around the medium) with the derived curves (see Fig. 1b).

reflection expected from the simulation. Regarding the green curve t_{10} , it is not possible to predict such a curve without knowing the internal structure of the investigated medium and it is very important to be aware of similar unexpected reflections to prevent possible misinterpretations.

3. Laboratory measurements

3.1. Setup

In order to further investigate transmission curves which can be observed in cylinders, we performed radar measurements in laboratory conditions. The radar system and antennas play an additional role compared to the numerical experiments. Moreover, inherent heterogeneities in the real world are also expected to influence the radar measurements. For comparison purposes, we used the same experimental setup as in our previous study [25]. We created a simplified laboratory tree model made from plastic and cardboard pipes (see Fig. 14). The larger pipe was filled with sand to represent a lossless medium and the smaller pipe stayed empty to represent a void.

3.2. Radar system

For the radar measurements, we used two Vivaldi antennas [37], constructed at the Université catholique de Louvain, Belgium. The antennas were made of aluminium and their size was $24 \times 20 \times 2$ cm. A vector network analyser (VNA, ZVH 8, Rhode & Schwarz, Munich, Germany) was used as GPR system. The antennas were connected to the VNA with two 50Ω impedance coaxial cables of a length of 2.5 m. The operating frequency range was set to 0.8–3 GHz with a 2 MHz frequency step. The tools are shown in Fig. 15. In order to filter the GPR images, the zero spatial frequency was removed (average background subtraction). Again, for all our GPR images, we applied an exponential gain function. The measurements were carried out every 2 cm along the model circumference by performing separated static data acquisitions.

3.3. Radar results

In Fig. 16 the GPR image obtained with the use of the single-offset bistatic radar system is displayed. Compared to the numerical simulations, the reflections are shifted by approximately 1 ns because of the propagation inside the antennas. Nevertheless, the shapes of the reflection curves correspond to the analytical curves and those in the numerical simulations. The reflection curve highlighted by the green arrow corresponds to the straight-ray propa-

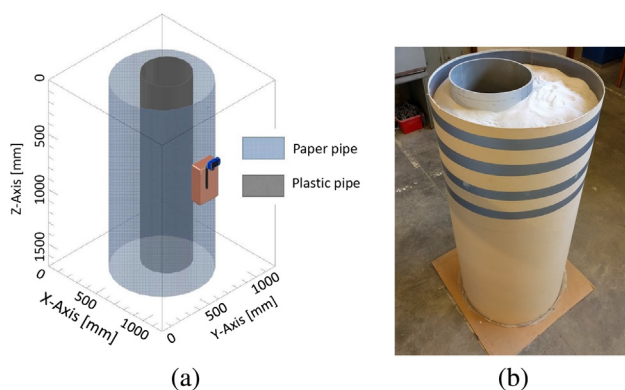


Fig. 14. The laboratory model: (a) 3-D design, (b) photo of the assembled model filled with sand.

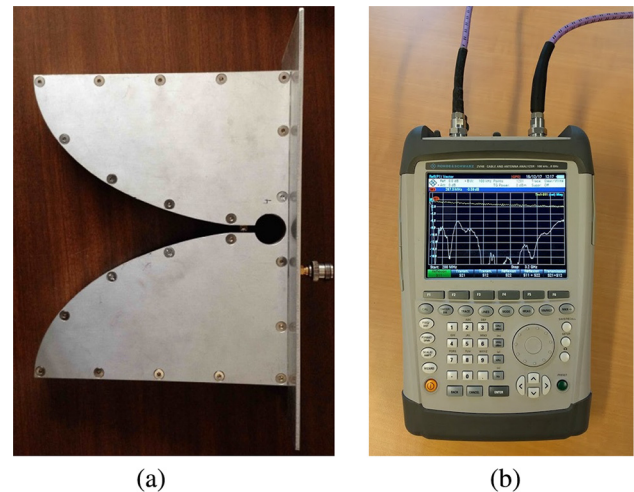


Fig. 15. (a) Vivaldi antenna [37] for the frequency range 0.8–3 GHz, (b) Handheld vector network analyser (VNA) used as frequency-domain radar system.

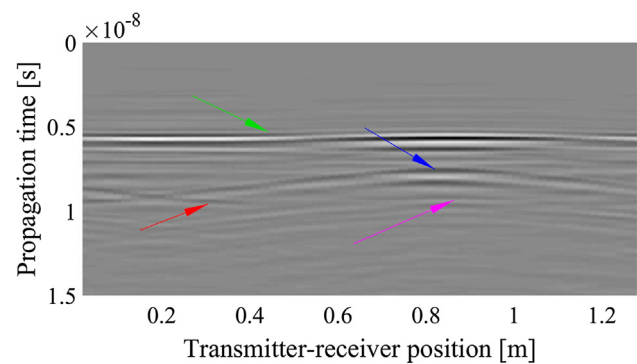


Fig. 16. Radar image of the first bistatic radar measurement with two antennas rotating around the laboratory model (see Fig. 1a).

gation shown in Fig. 6a. It is the strongest curve in the GPR image unlike the equivalent curve in the simulated GPR image in Fig. 4. This reflection is also much less linear than the simulated and the analytical ones. It is because of the inherently inhomogeneous character of the medium and antenna effects, including multiple internal reflections as well as antenna-medium coupling. The following curve (pointed out by the red arrow) is also much better visible than the one in the simulated GPR image. This curve, corresponding to the propagation path displayed in Fig. 6b, is more clearly visible when the receiver is relatively close to the void. It could receive easily the signal reflected from the void (in the GPR image, the curve is clear from 0 to 0.4 m). The next reflection curve, highlighted by the blue arrow and corresponding to the propagation path in Fig. 6c, is very well visible for all transmitter-receiver positions. The last reflection is the TIR, which is slightly visible at 9 ns and 0.8 m in Fig. 16 (see the magenta arrow).

Fig. 17 shows that the reflection curves appearing in the GPR image for the first case of the bistatic radar system have comparable shapes to the derived reflection curves and to the numerical simulations. However, the intensity of the reflections was very different in comparison with the simulated GPR image. The TIR is much less visible in the real data due to several factors: 1) the radiation pattern of the antenna is different than the source point in the numerical simulations, 2) air gaps between the antenna and the medium change the direction of the propagation paths, 3) wave propagation is influenced by inherent sand heterogeneities. The reflections from the internal void are, however, particularly stron-

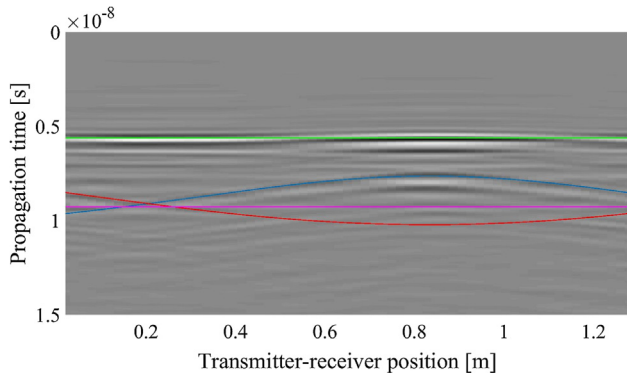


Fig. 17. Radar image of the first bistatic radar measurement with two antennas rotating around the laboratory model with the derived curves 1 ns shifted (see Fig. 1a).

ger than those in the simulated images because they are not overshadowed by the TIR. Unlike in the numerical simulations, in the real radar measurements we can observe many multiple reflections and a significant noise. Therefore, it was not straightforward to determine all the reflection curves observed in the numerical simulations.

Fig. 18 shows the second case of the bistatic radar measurement. Again, it is shifted by approximately 1 ns compared to the simulated images due to the different data acquisition (cable and antenna influence and grMax2D time shift). The blue arrow points at the reflection curve which is the strongest one in this GPR image and which corresponds to the propagation path displayed in Fig. 11a. The shape of the reflection is very similar to the derived one and it is nearly the same as the simulated one. Another reflection curve highlighted by the cyan arrow corresponds to the propagation path shown in Fig. 11b. It also agrees very well with the cyan curve derived in Fig. 12 and as well as the corresponding curve in the simulated GPR image. It appears more clearly in intervals 0–0.8 m and 1.6–2.5 m which correlate with the refracted signal (propagating through 2 media). The following reflection curve originating from the propagation path displayed in Fig. 11c is highlighted by the magenta arrow. The reflection is only very slightly visible due to the noisy background. The next reflection curves are those corresponding to the TIR. In Fig. 18 they are pointed out by the red and orange curves, respectively, as well as the TIR displayed in the simulated GPR image in Fig. 10 and in the analytical expression of the GPR image in Fig. 12. In the real GPR image, the TIR also appears as a diagonal cross and can, therefore, be readily identified. Nevertheless, the strength of the reflection is much weaker than the one in the sim-

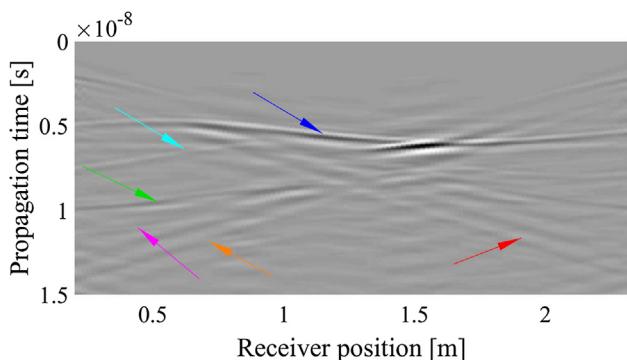


Fig. 18. Radar image of the second bistatic radar measurement with one transmitting antenna at a fixed position and one receiving antenna rotating around the laboratory model (see Fig. 1b).

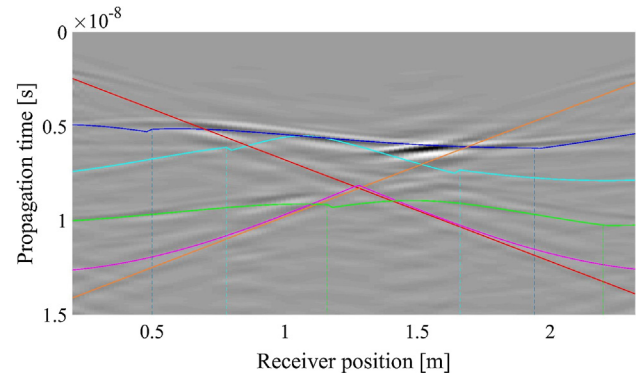


Fig. 19. Radar image of the second bistatic radar measurement with one transmitting antenna at a fixed position and one receiving antenna rotating around the laboratory model with the derived curves 1 ns shifted (see Fig. 1b).

ulated image. The last reflection pointed out by the green arrow is the second strongest reflection in Fig. 18. This reflection is also slightly visible in the simulated GPR image in Fig. 10. The origin of this reflection is nevertheless very complex (see the propagation path in Fig. 11e) and without careful analysis of the electric field distribution dynamics, it would not be possible to determine it.

The GPR images obtained by the real bistatic radar measurements turned out to have their shapes comparable to the ones obtained by the numerical simulations and the derived ones which are presented in Fig. 19. However, the intensities of the reflection curves varied. The reflection curves described by the straight-ray propagation were more remarkable than the TIR due to the antenna-medium interaction described above.

As well as for the numerical simulations, the second case of the bistatic radar measurement provided a more complex GPR image providing valuable information about the investigated medium. Some reflection curves (notably the first and the second) give us knowledge about the internal structure of the medium with their shape. Other reflections (notably the TIR) give us information about general electromagnetic properties of the medium with their propagation time value. It is worth to know that it is possible to observe other reflections (notably the last one) which can appear very strongly. Nevertheless, without knowing the internal structure it is not very likely to describe reflections correctly, which can lead to misinterpretations of the investigated medium.

4. Case studies

In order to analyse more complex cases, we performed radar measurements around two different cylindrical objects, namely, a reinforced concrete column and a tree trunk with a cavity. We used the same radar system as for the laboratory experiment. Again, we removed zero spatial frequency to filter the images and we used an exponential gain function to compensate for signal attenuation with respect to propagation time. In order to compare different methods, three GPR measurements were done: 1) monostatic radar measurement with one antenna rotating around the column, 2) bistatic radar single-offset measurement with two antennas rotating around the column with fixed distance, and 3) bistatic radar multi-offset measurement with one standing transmitting antenna and one receiving antenna which was rotating around the column.

4.1. Concrete column inspection

4.1.1. Setup

The reinforced concrete column under test was manufactured by the company Ergon nv/sa in Lier, Belgium. The column and its

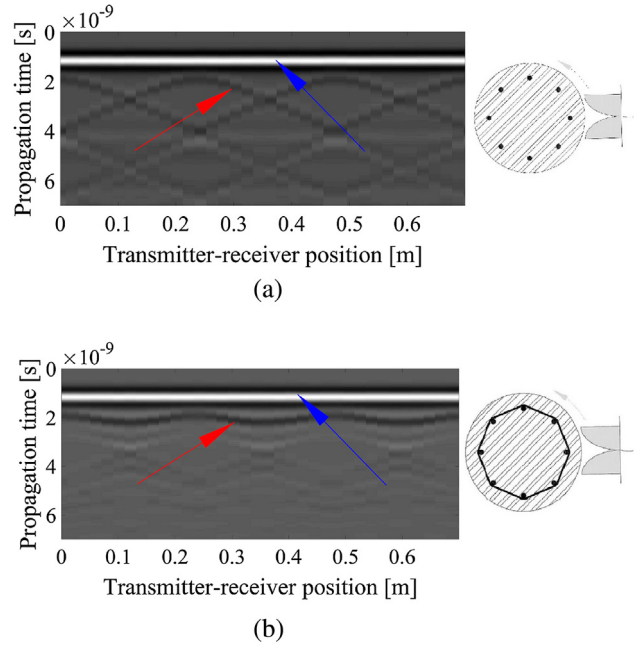
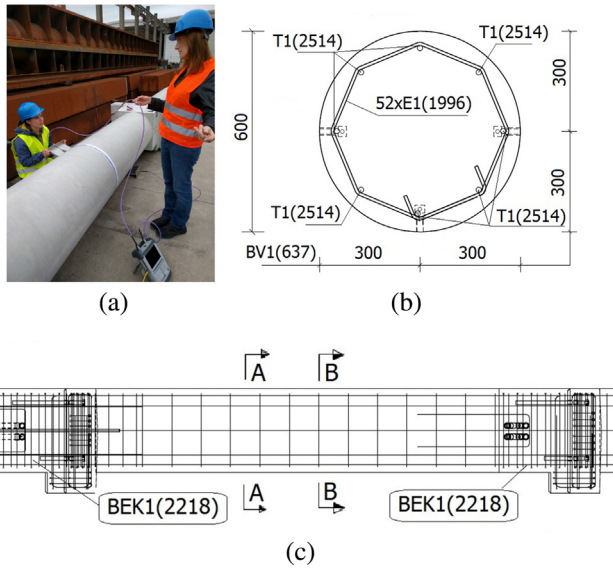


Fig. 20. Concrete column: (a) radar measurement of the column, (b) transverse cross-section of the column, (c) Longitudinal cross-section of the column. Ergon nv/ sa in Lier, Belgium.

Fig. 22. Numerical simulations of the concrete column reinforcement in grpMax2D. The blue arrow points at the surface reflection and the red arrow points at the rebar reflection: (a) longitudinal reinforcement (cross section A in Fig. 20c) – series of hyperbolas, (b) longitudinal and transverse reinforcement (cross section B in Fig. 20c) – continuous periodic corrugated curve. (For interpretation of the references to colour in this figure legend, the reader is referred to the web version of this article.)

cross-section are displayed in Fig. 20. The diameter of the column was 0.6 m and it was longitudinally reinforced by 8 steel bars T1 (\varnothing 25 mm) which were stabilized every 210 mm by a circular transverse reinforcement E1 (\varnothing 8 mm). Because of the limited accessibility of the antennas to the column (see Fig. 21), only a part of the column was investigated (\approx 1.5 m of the circumference).

4.1.2. Numerical simulations

In order to provide insights into the structure of the radar images for that column, simulations with grpMax2D were performed before the measurements. Fig. 22 shows the first 7 ns of the simulated GPR images obtained for two arrangements of the reinforcing bars. Apart from the surface reflection (blue arrows), we can see the reflections from the rebars (red arrows) which are very different for each arrangement. Fig. 22a shows the rebars as a series of reflection hyperbolas, whereas Fig. 22b displays them as a continuous periodic corrugated curve.

4.1.3. Radar results

In Fig. 24a the GPR image obtained with the monostatic radar system (one antenna) is displayed. It is a relatively complex radargram with many multiple reflections. Nevertheless, it shows several strong reflection curves. The first reflection pointed out by the red arrow between 3 and 4 ns was caused by the steel rein-

forcement in the column. The corrugated appearance of this reflection corresponds to the reflection from the transverse ring rather than the longitudinal rebars which would appear as a series of hyperbolas as in Fig. 22a. The blue arrows highlight the reflection from the ground at the beginning and at the end of the measurement. In the middle of the radargram, several strong reflections are displayed and pointed out by the green arrow. These reflections originate from external interferences from the metallic structure close to the column (see Figs. 20a and 21). In the GPR image, the reflection curve showing the other side of the column is missing due to the very complex signal propagation between the reinforcing bars. Furthermore, the TIR is not visible because of the antenna-medium interactions described in Section 3.

Fig. 23 shows an example of the GPR image without any image processing (gain function, zero spatial frequency removal). This radargram was obtained by a monostatic radar system applied

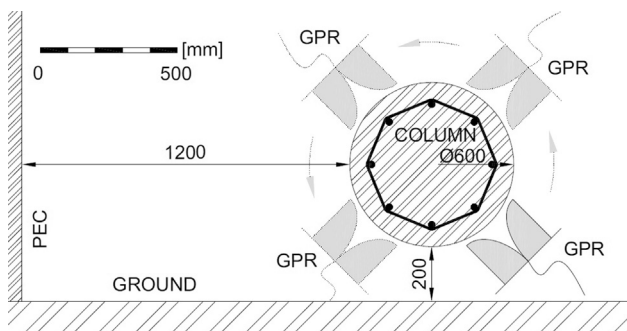


Fig. 21. Access of the antennas to the reinforced concrete column for the monostatic and bistatic data acquisition schemes.

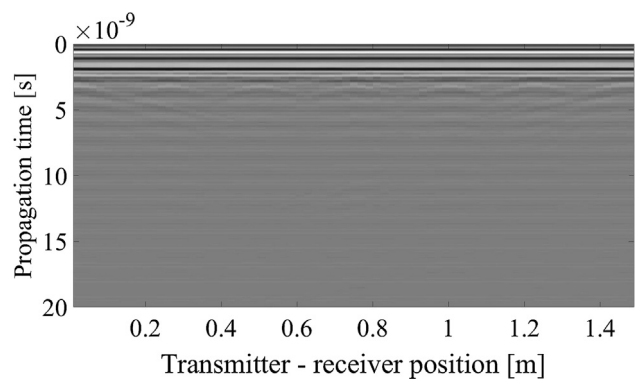


Fig. 23. Example of a radargram of the concrete column obtained with a monostatic radar system without any data processing. The corresponding radar image after data processing is shown in Fig. 24a.

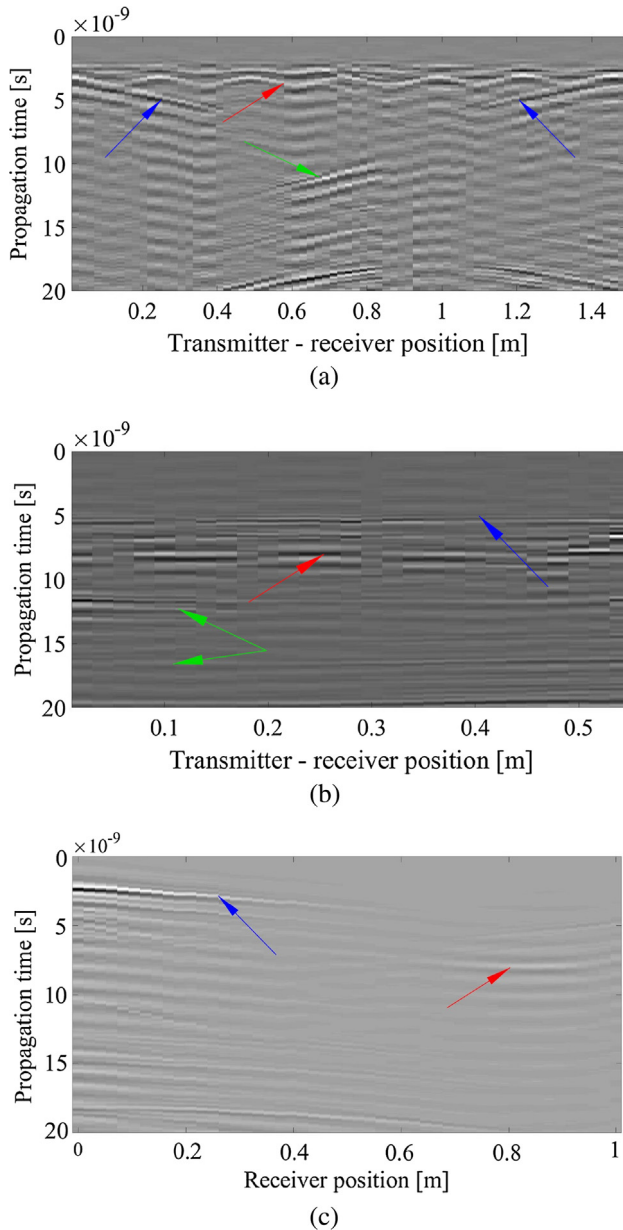


Fig. 24. Radar measurement of the concrete column: (a) monostatic system with one antenna, (b) bistatic single-offset system with two rotating antennas, (c) bistatic multi-offset system with the static transmitter and the rotating receiver.

on the concrete column. The corresponding processed GPR image is displayed in Fig. 24a.

In Fig. 24b the first case of the bistatic radar measurement is shown. Also in this case, a lot of clutter is present, but the first, though not the strongest, reflection which is highlighted by the blue arrow (5,5 ns) is the straight-ray signal which points at the opposite side of the column. Unlike the previous radargram, which shows mainly the transverse ring, it proves that the signal can really propagate through the column. The second reflection curve pointed out by the red arrow (8 ns) is the TIR. It is regularly discontinuous which points at the metallic bars distribution influencing the strength of the electric field. Fig. 25 shows a simulated distribution of the electric field in the reinforced concrete column for two transmitter–receiver positions ($\theta = 0^\circ$ and $\theta = 25^\circ$) for the propagation time 7,1 ns (numerical simulations and case studies were approximately 1 ns shifted because of the propagation in

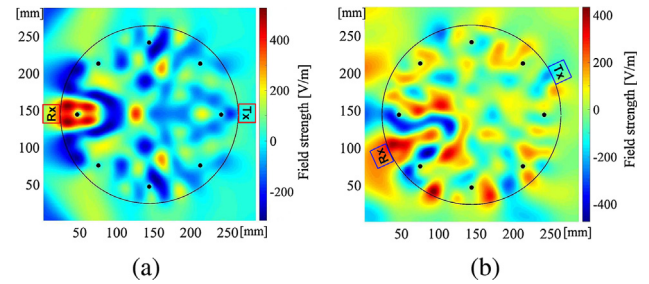


Fig. 25. Numerical simulation in gprMax2D. Distribution of electromagnetic field in the concrete column at 7,1 ns for antennas positions: (a) $\theta = 0^\circ$, (b) $\theta = 25^\circ$.

the antenna). The values of the electric field strength were not normalized in this case, so we can observe the differences caused by the column reinforcement. The position of the TIR provides information about the relative permittivity of the medium. Considering the beginning of propagation in the medium (1–1,5 ns according to the surface reflection in Fig. 24a), the propagation time of the TIR in the medium is 6,5–7 ns. Using Eq. (2) and knowing the diameter of the column $D = 0,6$ m (then, the distance $d = 0,6 \cdot \pi/2$), the relative permittivity of the column is $\epsilon_r = 4,2$ –4,9. In this GPR image, a multiple reflection of the opposite side of the column is visible at 11 ns and 16,5 ns (green arrows).

Finally, the last GPR image obtained by the bistatic radar system in the multi-offset mode is displayed in Fig. 24c. This measurement was performed for approximately one half of the circumference due to the column accessibility. In this radargram, the strongest reflection highlighted by the blue arrow is the direct wave between the two antennas which are relatively close to each other. This reflection is progressively weaker when the antennas are further from each other. When the antennas are approximately opposite to each other, we can observe a reflection curve pointing at the opposite side of the column (red arrow). This measurement was not very useful for the rebars detection because the medium appears to be homogeneous according to this radargram.

For the concrete column inspection, the monostatic radar system turned out to be the most straightforward for data interpretation. The rebars were detected quite precisely, despite the fact that it is not clear without previous knowledge where is the position of the transverse ring. In that respect, the bistatic single-offset radar measurement proved that the signal is able to propagate through the rebars and so, the transverse reinforcement is not present all along the whole length of the column (only in certain intervals). In this case, the TIR is visible and so, it can be used to determine relative permittivity ϵ_r of the medium ($\epsilon_r = 4,2$ –4,9). The GPR image from the last measurement did not show a lot of information and so, it is not recommended to use it for this application.

4.2. Tree trunk measurement

4.2.1. Situation

We performed monostatic and bistatic radar measurements on a lime tree (*Tilia cordata*) situated in the city centre of Ottignies, Belgium (see Fig. 26a). The tree was situated in a highly populated area. The circumference of the tree trunk was 2,99 m at the height of 0,4 m above the ground. The height of the tree was about 19 m. For comparison purposes, ultrasonic measurements were also acquired around the tree trunk.

4.2.2. Ultrasonic tomography

This tree was inspected with an ultrasonic tomography by Martin Cléda from the Walloon public service (Direction Ressources forestières – Cellule “Arbres remarquables”). The data acquisition

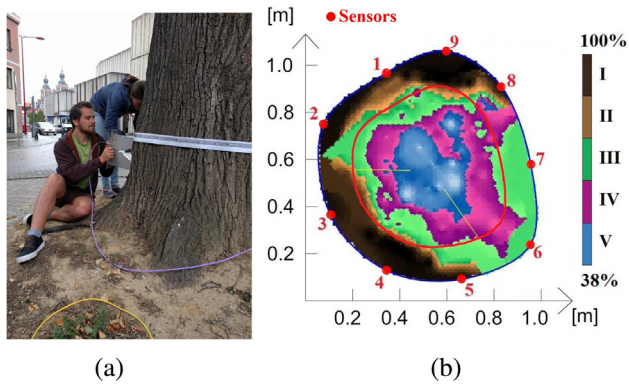


Fig. 26. The investigated tree trunk: a) during the radar measurement (bistatic radar system with the static transmitter and the rotating receiver), b) result of the ultrasonic tomography (PiCUS Sonic Tomograph) obtained by Martin Cléda (Walloon public service). The color bar indicates states of wood in relative velocities: (I) 90–100%: healthy wood, (II) 80–90%: healthy wood, (III) 70–80%: early wood degradation, (IV) 60–70%: wood degradation, (V) <60%: wood degradation/cavity.

was performed with 9 ultrasonic sensors (all of them were transmitters and receivers at the same time) placed at the whole length of the trunk circumference every ≈ 35 cm. Each sensor/point was tested 3 times with a little hammer. The sonic sensors receive the acoustic wave and record its velocity in [m/s] which is dependent on wood density and elasticity. Thus, the speed of the elastic waves in wood correlates with its quality. In Fig. 26b, the results of the ultrasonic tomography (PiCUS Sonic Tomograph, ARGUS Electronic GmbH, Rostock, Germany) are shown. The color bar shows the relative velocities [%], where 100% is the quickest measured velocity. It pointed at the state of wood which included the presence of 33% of healthy wood and 40% of cavities. The red line signifies a theoretical threshold of the rupture risk.

4.2.3. Radar results

In Fig. 27a the first GPR image of the tree trunk is presented. It was obtained using the monostatic radar system as in the previous cases. The most particular element in the radargram is the surface reflection (blue arrow) which is very strong due to the large difference between the relative permittivity of air ($\epsilon_r \approx 1$) and living wood ($\epsilon_r \approx 10$ –15 depending on a tree species and other factors). High moisture of living wood also causes high electrical conductivity and thus, the signal is strongly attenuated. Therefore, the GPR image is not very clear and we cannot observe many reflections. Nevertheless, several reflections are visible around 10 ns in some parts of the image (red arrows). They are joint in the positions 0–1,2 m and 2,7–3 m, out of these intervals (1,2–2,7 m) they are attenuated. These reflections point at certain inhomogeneities inside the tree trunk which are closer to the bark in positions corresponding to those with visible internal reflections. The TIR is not visible in the radargram because the tree trunk is very rough and so, the internal reflections have complex propagation paths. Furthermore, the signal is strongly attenuated in living wood, thus, it is very complicated to record and recognize it.

The GPR image displayed in Fig. 27b presents results obtained with the single-offset bistatic radar system. The first visible reflection pointed out by the green arrow (9–10 ns) is the straight-ray propagation between the antennas and it shows the opposite side of the trunk. Then, in this GPR image, we can observe mainly multiple reflections. Nevertheless, the homogeneity of the radargram is disrupted by two positions pointed out by the red and the blue arrows. Because the reflections in the radargram are not evenly distributed, it is certain that an inhomogeneity (e.g., a cavity) in

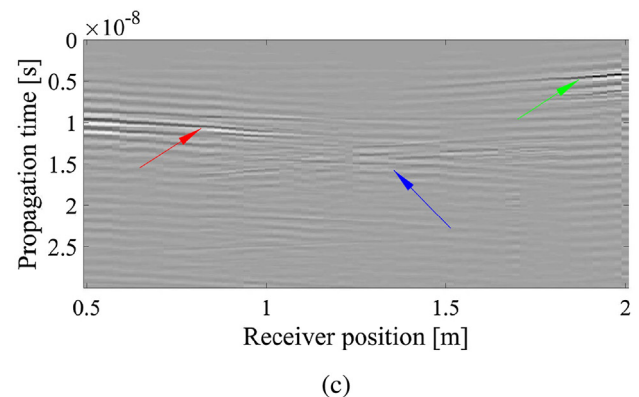
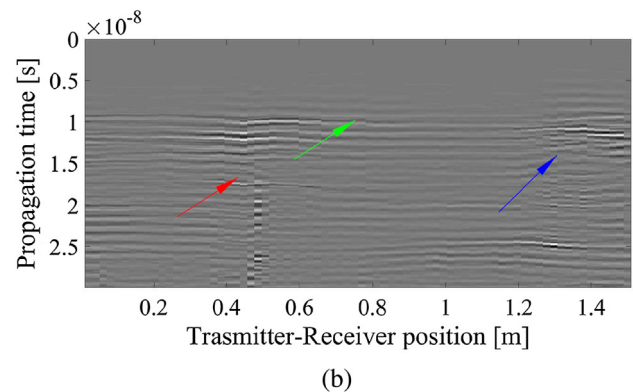
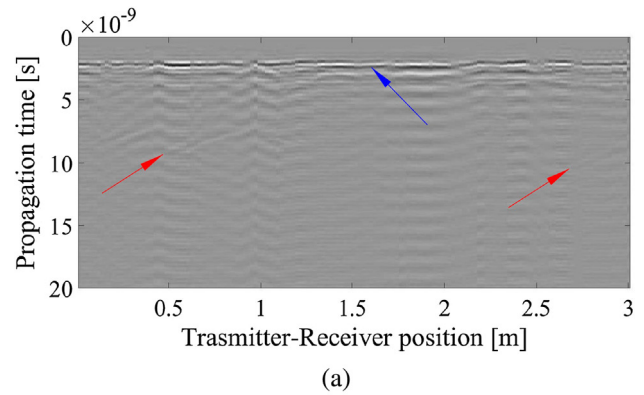


Fig. 27. Radar measurement of the tree trunk: (a) Monostatic system with one antenna, (b) bistatic single-offset system with two rotating antennas, (c) bistatic multi-offset system with the static transmitter and the rotating receiver.

the tree trunk is present. As well as in the previous case, the TIR is missing in this radargram.

Fig. 27c represents the third radar measurement performed with the bistatic radar system with one static transmitting antenna and one receiving antenna rotating around the tree. From the image, just a short part (0.5–2 m) was taken because the direct signal between the two antennas was too strong and the rest of the radargram was too attenuated. The green arrow points at the direct signal propagation between the antennas along the edge of the trunk. Nevertheless, the red and the blue arrows highlight certain internal inhomogeneities in the trunk similarly to the previous case.

The ultrasonic tomography provided a map of the wood properties based on the velocities of the ultrasonic waves transmitted from each sonic sensors to the others. This technique is very well developed and it has been used for several years. We have, on the other hand, demonstrated a usage of GPR imaging which is

a novel and promising technology that might provide a detailed map of trees permittivities in future. Nevertheless, this technique requires a lot of development to be fully used. The GPR inspections of the tree trunk revealed a series of heterogeneities within the trunk. The moisture of living wood is relatively high, therefore the signal is strongly attenuated and we cannot observe the internal structure in detail. Nevertheless, we are able to say that an area with very different electromagnetic properties is present inside the tree trunk.

5. Summary and conclusions

Two configurations of a bistatic radar system were used and compared in this paper in order to better understand the reflection curves occurring in cylindrical objects. In Section 2, a cylindrical structure was observed using the numerical simulations with the *gprMax2D* software. Then, several possible propagation paths were analysed in order to analytically derive reflection curves in GPR images for cylindrical structures. Knowing the shape and the position of such curves helps to understand other GPR images of unknown structures. The results showed a very good agreement with respect to the analytically derived reflection curves using the straight-ray propagation assumption. The reflection curves obtained by numerical simulations had much smoother shape though. In both cases, the TIR was the dominant reflection curve which gave us information about the velocity of the propagation and so, about electromagnetic properties of the medium. Nevertheless, it made the other reflections weaker and thus, the inhomogeneous internal structure of the medium could not be accurately determined (especially for the single-offset bistatic mode). To compare the simulations and the analytical curves, laboratory measurements over a tree trunk model were done. The GPR images obtained by these measurements were very similar to the numerical simulations and also to the schematic expressions. Nevertheless, the intensity of the curves appeared much stronger for the direct path and much weaker for the TIR due to the antenna effects and antenna-medium interactions.

This phenomenon could be caused by the fact that the simulation software assumes ideal conditions and so, the TIR is indeed total. Hence, the reflection is very strong and overshadows the other reflections which are normally more prominent. On the other hand, in real conditions the TIR is weaker due to several factors: 1) the radiation pattern of the antenna is different than the source point in the numerical simulations, 2) air gaps between the antenna and the medium change the direction of the propagation path, 3) signal may be influenced by local sand heterogeneities. Therefore, in the laboratory measurements, the TIR appears weaker compared to the direct path. The positions and the shapes of the curves were in good agreement, even though they were slightly shifted due to the use of a different kind of methods. The analytical formulas neglected all the effects related to the source. The simulations assume a point source, while the measurements were done using Vivaldi antennas. We provided the analytical expressions of the transmission curves occurring in a cylinder containing a cylindrical object.

While comparing the two bistatic radar measurements, the first one (single-offset) appears to be very simple, whereas the second one (multi-offset) seems to be very complex and information-rich. However, due to its complexity, it is not possible to correctly interpret every reflection curve without the prior knowledge of the internal structure. This fact can lead to misinterpretations of the GPR image.

The static data acquisition provides very precise positioning of the data, nevertheless, it is more time consuming. While using a continuous measurement, a positioning system is needed and

the single-offset bistatic radar system is not possible to perform precisely due to the unsynchronized movement of the two antennas.

The case studies demonstrate the benefit of the combination of the monostatic and the bistatic radar system for studying cylinders. While using the bistatic system, we are able to obtain information which would not be available from the monostatic radar measurement. For example, while using the monostatic system on the concrete column, we were able to see only the transverse reinforcement close to the surface and nothing behind it. On the other hand, while using the bistatic system, we could see through the longitudinal reinforcement and thus investigate the core of the column.

The investigation of the tree showed that the bistatic system is able to detect irregularities in the tree trunk. Detailed investigation of this tree trunk by an ultrasonic tomography revealed that those inhomogeneities probably corresponds to a hole. And thus, this system can be used to indicate candidates for detailed investigations. Concerning the quality of the radar tree trunk tomography, it is still being developed, therefore the results are not as information-rich as other techniques (e.g., ultrasonic tomography). However, GPR is a device with the future prospects of being relatively quick.

Conflict of interest

None declare.

Acknowledgment

The authors would like to acknowledge the support of the Fonds de la Recherche Scientifique (FNRS), Belgium, through the SENSWOOD project (Convention n° 19526260). This research was also carried out within the framework of EU funded COST Action TU 1208 “Civil Engineering Applications of Ground Penetrating Radar”. The authors are also very grateful that the company ERGON nv/sa in Lier, Belgium provided the concrete column for the GPR inspection. Finally, authors would like to thank Martin Cléda from the Walloon public service (Direction Ressources forestières – Cellule “Arbres remarquables”) for providing the ultrasonic tomography scans.

References

- [1] D.J. Daniels, *Ground Penetrating Radar*, IEE, second ed., ISBN: 0863413609, 2004.
- [2] J.J. Daniels, *Ground penetrating radar fundamentals*, Prepared as an appendix to a report to the U.S.EPA, Region V.
- [3] A.P. Annan, *GPR – history, trends, and future*, *Subsurf. Sens. Technol. Appl.* 3 (4) (2002) 253–270.
- [4] A.M. Alani, F. Tosti, *Gpr applications in structural detailing of a major tunnel using different frequency antenna systems*, *Constr. Build. Mater.*
- [5] M. Solla, H. Lorenzo, F. Rial, A. Novo, *Ground-penetrating radar for the structural evaluation of masonry bridges: results and interpretational tools*, *Constr. Build. Mater.* 29 (2012) 458–465.
- [6] A. Benedetto, F. Tosti, L.B. Ciampoli, F. D’Amico, *An overview of ground-penetrating radar signal processing techniques for road inspections*, *Signal Process.* 132 (Supplement C) (2017) 201–209.
- [7] J. Minet, P. Bogaert, M. Vanclooster, S. Lambot, *Validation of ground penetrating radar full-waveform inversion for field scale soil moisture mapping*, *J. Hydrol.* 424–425 (Supplement C) (2012) 112–123.
- [8] F. Jonard, L. Weihermüller, H. Vereecken, S. Lambot, *Accounting for soil surface roughness in the inversion of ultrawideband off-ground GPR signal for soil moisture retrieval*, *Geophysics* 77 (1) (2012) H1–H7.
- [9] M.R.M. Ardekani, D.C. Jacques, S. Lambot, *A layered vegetation model for GPR full-wave inversion*, *IEEE J. Sel. Top. Appl. Earth Obs. Remote Sens.* 9 (1) (2016) 18–28.
- [10] F. André, C. van Leeuwen, S. Saussez, R.V. Durmen, P. Bogaert, D. Moghadas, L. de Ressaiguier, B. Delvaux, H. Vereecken, S. Lambot, *High-resolution imaging of a vineyard in south of france using ground-penetrating radar, electromagnetic induction and electrical resistivity tomography*, *J. Appl. Geophys.* 78 (Supplement C) (2012) 113–122.

- [11] K. Labropoulos, A. Moropoulou, Ground penetrating radar investigation of the bell tower of the church of the holy sepulchre, *Constr. Build. Mater.* 47 (2013) 689–700.
- [12] V. Pérez-Gracia, F. García, L.G. Pujades, R.G. Drigo, D.D. Capua, GPR survey to study the restoration of a roman monument, *J. Cult. Heritage* 9 (1) (2008) 89–96.
- [13] S. Santos-Assunção, V. Pérez-Gracia, O. Caselles, J. Clapes, V. Salinas, Assessment of complex masonry structures with GPR compared to other non-destructive testing studies, *Remote Sens.* 6 (9) (2014) 8220–8237.
- [14] M. Zajc, Ž. Pogačnik, A. Gosar, Ground penetrating radar and structural geological mapping investigation of karst and tectonic features in flyschoid rocks as geological hazard for exploitation, *Int. J. Rock Mech. Min. Sci.* 67 (Supplement C) (2014) 78–87.
- [15] A. Bernatek-Jakiel, M. Kondracka, Combining geomorphological mapping and near surface geophysics (GPR and ERT) to study piping systems, *Geomorphology* 274 (Supplement C) (2016) 193–209.
- [16] M. Elkarmoty, C. Colla, E. Gabrielli, P. Papeschi, S. Bonduà, R. Bruno, In-situ gpr test for three-dimensional mapping of the dielectric constant in a rock mass, *J. Appl. Geophys.* 146 (Supplement C) (2017) 1–15.
- [17] J. Ježová, S. Lambot, Reflection waveforms occurring in GPR tree trunk testing, 2016 16th International Conference on Ground Penetrating Radar (GPR), 2016, pp. 1–5.
- [18] I. Al-Qadi, S. Lahouar, Measuring rebar cover depth in rigid pavements with ground-penetrating radar, *Transp. Res. Rec.* 2005 (1907) 81–85.
- [19] O. Lopera, E.C. Slob, N. Milisavljević, S. Lambot, Filtering soil surface and antenna effects from gpr data to enhance landmine detection, *IEEE Trans. Geosci. Remote Sens.* 45 (3) (2007) 707–717. cited By:47 Export Date: 9 June 2015.
- [20] G.D. Donno, L.D. Giambattista, L. Orlando, High-resolution investigation of masonry samples through GPR and electrical resistivity tomography, *Constr. Build. Mater.* 154 (Supplement C) (2017) 1234–1249.
- [21] A. Ristić, Ž. Bugarinović, M. Vrtunski, M. Govedarica, D. Petrovački, Integration of modern remote sensing technologies for faster utility mapping and data extraction, *Constr. Build. Mater.* 154 (Supplement C) (2017) 1183–1198.
- [22] F. Garcia-García, A. Valls-Ayuso, J. Benloch-Marco, M. Valcuende-Paya, An optimization of the work disruption by 3d cavity mapping using GPR: a new sewerage project in torrente (valencia, spain), *Constr. Build. Mater.* 154 (Supplement C) (2017) 1226–1233.
- [23] A. Ciampalini, F. André, F. Garfagnoli, G. Grandjean, S. Lambot, L. Chiarantini, S. Moretti, Improved estimation of soil clay content by the fusion of remote hyperspectral and proximal geophysical sensing, *J. Appl. Geophys.* 116 (Supplement C) (2015) 135–145.
- [24] J. Zhang, H. Lin, J. Doolittle, Soil layering and preferential flow impacts on seasonal changes of GPR signals in two contrasting soils, *Geoderma* 213 (Supplement C) (2014) 560–569.
- [25] J. Ježová, L. Mertens, S. Lambot, Ground-penetrating radar for observing tree trunks and other cylindrical objects, *Constr. Build. Mater.* 123 (2016) 214–225.
- [26] L. Nuzzo, T. Quarta, GPR prospecting of cylindrical structures in cultural heritage applications: a review of geometric issues, *Near Surf. Geophys.* 10 (2012) 17–34.
- [27] N. Bonomo, D. Bullo, A. Villela, A. Osella, Ground-penetrating radar investigation of the cylindrical pedestal of a monument, *J. Appl. Geophys.* 113 (2015) 1–13.
- [28] R. Persico, G. Gennarelli, F. Soldovieri, Gpr prospecting on circular surfaces: preliminary results, in: *Proceedings of the 15th International Conference on Ground Penetrating Radar, 2014*, pp. 79–82.
- [29] G. Leucci, R. Cataldo, G.D. Nunzio, Assessment of fractures in some columns inside the crypt of the cattedrale di otranto using integrated geophysical methods, *J. Archaeol. Sci.* 34 (2) (2007) 222–232.
- [30] G. Leucci, R. Persico, F. Soldovieri, Detection of fractures from GPR data: the case history of the Cathedral of Otranto, *J. Geophys. Eng.* 4 (2007) 452–461.
- [31] G. Nicolotti, L.V. Socco, R. Martinis, A. Godio, L. Sambuelli, Application and comparison of three tomographic techniques for detection decay in trees, *J. Arboric.* 29 (2) (2003) 66–78.
- [32] H. Lorenzo, V. Pérez-Gracia, A. Novo, J. Armesto, Forestry applications of ground-penetrating radar, *For. Syst.* 19 (1) (2010) 5–17.
- [33] S.A. Al Hagrey, Geophysical imaging of root-zone, trunk, and moisture heterogeneity, *J. Exp. Bot.* 58 (4) (2007) 839–854.
- [34] A. Giannopoulos, Modelling ground penetrating radar by GprMax, *Constr. Build. Mater.* 19 (10) (2005) 755–762.
- [35] C. Warren, A. Giannopoulos, I. Giannakis, GprMax: open source software to simulate electromagnetic wave propagation for ground penetrating radar, *Comput. Phys. Commun.* 209 (2016) 163–170.
- [36] A. Taflove, S.C. Hagness, M. Piket-May, 9 – computational electromagnetics: the finite-difference time-domain method, in: W.-K. Chen (Ed.), *The Electrical Engineering Handbook*, Academic Press, Burlington, 2005, pp. 629–670.
- [37] R. Sarkis, C. Craeye, Circular array of wideband 3d vivaldi antennas, in: *2010 URSI International Symposium on Electro- magnetic Theory, 2010*, pp. 792–794.